

# Does deep learning model calibration improve performance in class-imbalanced medical image classification?

Sivaramakrishnan Rajaraman <sup>1\*</sup>, Prasanth Ganesan <sup>2</sup>, Sameer Antani <sup>1</sup>

<sup>1</sup> National Library of Medicine, National Institutes of Health, Bethesda, MD 20814, United States of America

<sup>2</sup> Stanford University Department of Medicine, Stanford, CA 94305, United States of America

\* Correspondence: [sivaramakrishnan.rajaraman@nih.gov](mailto:sivaramakrishnan.rajaraman@nih.gov); Tel.: +1-301-827-2383

## Abstract

In medical image classification tasks, it is common to find that the number of normal samples far exceeds the number of abnormal samples. In such class-imbalanced situations, reliable training of deep neural networks continues to be a major challenge. Under these circumstances, the predicted class confidence may be biased toward the majority class. Calibration has been suggested to alleviate some of these effects. However, there is insufficient analysis explaining when and whether calibrating a model would be beneficial in improving performance. In this study, we perform a systematic analysis of the effect of model calibration on its performance on two medical image modalities, namely, chest X-rays (CXRs) and fundus images, using various deep learning classifier backbones. For this, we study the following variations: (i) the degree of imbalances in the dataset used for training; (ii) calibration methods; and, (iii) two classification thresholds, namely, default decision threshold of 0.5, and optimal threshold from precision-recall (PR) curves. Our results indicate that at the default operating threshold of 0.5, the performance achieved through calibration is significantly superior ( $p < 0.05$ ) to an uncalibrated model. However, at the PR-guided threshold, these gains were not significantly different ( $p > 0.05$ ). This finding holds for both image modalities and at varying degrees of imbalance.

**Keywords:** calibration; classification; chest-X-ray; data imbalance; decision threshold; deep learning; fundus images; error analysis; precision-recall curves.

## 1. Introduction:

Deep learning (DL) methods have demonstrated incredible gains in the performance of computer vision processes such as object detection, segmentation, and classification, which has led to significant advances in innovative applications [1]. DL-based computer-aided diagnostic systems have been used for analyzing medical images as they provide valuable information about the disease pathology. Some examples include chest X-rays (CXRs) [2], computed tomography (CT), magnetic resonance (MR), fundus images [3], cervix images [4], and ultrasound echocardiography [5], among others. Such analyses help in identifying and classifying disease

patterns, localizing and measuring disease manifestations, and recommending therapies based on the predicted stage of the disease.

The success of DL models is due to not only the network architecture but significantly due to the availability of large amounts of data for training the algorithms. In medical applications, we commonly observe that there is a high imbalance between normal (no disease finding) and abnormal data. Such imbalance is undesirable in training DL models. The bias introduced by class-imbalanced training is commonly addressed by tuning the class weights [6]. This step attempts to compensate for the imbalance by penalizing the majority class. However, this does not eliminate bias. Improvements in the accuracy of the minority class achieved through changes in class weights occur at the cost of reducing the performance of the majority class. Other widely followed techniques for handling class imbalance are data augmentation [7] and random under-sampling [8] that have demonstrated performance improvement in several studies. However, in scenarios where augmentation isn't applicable as it may adversely distort the data characteristics, model calibration may be applied for rescaling the class-confidence values and compensate for the imbalance.

Model calibration refers to the process of rescaling the class-confidence values predicted by the model to make them faithfully represent the true likelihood of occurrences of classes present in the training data [9]. For real-time decision-making, particularly in healthcare applications, the models are expected to be not only accurate but also to make predictions that are not over-or under-confident thereby establishing trustworthiness and reliability [10].

Several calibration methods have been proposed in the literature, such as Platt scaling, isotonic regression, beta calibration, spline calibration, and others [11], [12], [13]. A recent study used calibration methods to rescale the predicted probabilities toward text and image processing tasks [9]. The authors observed that the DL models trained with batch normalization layers demonstrated higher miscalibration. It was also observed that the calibration was negatively impacted while training with reduced weight decay. Another study [14] experimented with ImageNet, MNIST, Fashion MNIST, and other natural image datasets to analyze calibration performance through the use of adaptive probability binning strategies. They demonstrated that calibrated scores may or may not improve performance and it depends on the performance metric used to assess predictions. The authors of [15] used AlexNet [16], ResNet-50 [17], DenseNet-121 [18], and SqueezeNet [19] models as feature extractors to extract and classify features from four medical image datasets. The predicted probabilities are rescaled and mapped to their true likelihood of occurrence using a single-parameter version of Platt scaling. It was observed that the expected calibration error (ECE) decreased by 65.72% compared to that obtained with their uncalibrated counterparts while maintaining classification accuracy. In another study [20], the authors used the single-parameter version of Platt scaling to calibrate the confidence scores toward a multi-class polyp classification task. It was observed that the ECE and maximum calibration error (MCE) were reduced using calibrated probabilities and resulted in improved model interpretability. The authors of [21] used the single-parameter version of Platt scaling to calibrate probabilities obtained toward an immunofluorescence classification task using renal biopsy images. It was observed that the ECE

values reduced after calibration, however, it resulted in reduced accuracy, compared to their uncalibrated counterparts.

These studies establish that calibration reduces errors due to the mismatch between the confidence scores and the true likelihood of occurrence of the events. We observe that while the authors of [9], [14] conduct some experiments on calibration measurement, their works lack a detailed analysis of the relationship between the degree of data imbalance, the calibration methods, and the effect of the operating threshold on model performance before and after calibration. Until the time of writing this manuscript, to the best of our knowledge, no literature exists for class-imbalanced medical image classification tasks that investigates: (i) selection of calibration methods for superior performance; (ii) finding an optimal “calibration-guided” threshold for varying degrees of data imbalances; and, (iii) statistical significance of performance gains through the use of a threshold derived from calibrated probabilities over default operating threshold of 0.5.

In this study, we perform a detailed, systematic analysis to investigate if model calibration would help improve performance in class-imbalanced medical image classification tasks. We evaluate the model performance before and after calibration using two medical image modalities, namely, CXRs and fundus images. We used the Shenzhen TB CXRs [22] dataset and the fundus images made available by the Asia Pacific Tele-Ophthalmology Society (APTOS) for a Kaggle competition to detect diabetic retinopathy (DR). For these, we artificially vary the degrees of data imbalance in the training dataset such that the abnormal samples are 20%, 40%, 60%, and 80% proportions of normal samples. We used three different DL classifier backbone models, namely, VGG-16 [23], Densenet-121 [18], and Inception-V3 [24], which are shown to deliver superior performance in medical computer vision tasks. We evaluated the impact on the performance using three calibration methods, namely, Platt scaling, beta calibration, and spline calibration. Each calibration method is evaluated using log loss and ECE metrics. Finally, we studied the effect of two classification thresholds. One is the default decision threshold of 0.5, and the other is the optimal threshold derived from the precision-recall (PR) curves. The post-calibration performance is compared to that of the uncalibrated model for both the default classification threshold (0.5) and PR-guided optimal threshold.

The rest of the paper is organized as follows: Section II discusses the materials and methods used in this study, Section III shows the obtained results, and Section IV elaborates on the results and concludes the study.

## **2. Materials and Methods:**

### **2.1. Datasets characteristics**

The following datasets are used in this retrospective study:

(i) APTOS 2019 fundus images: A large-scale collection of fundus images obtained through fundus photography are made publicly available by the Asia Pacific Tele-Ophthalmology Society (APTOS) for the APTOS 2019 Blindness Detection challenge (<https://www.kaggle.com/c/aptos2019-blindness-detection/overview>). The goal of the challenge is to classify them as showing normal retina or signs of diabetic retinopathy (DR). Those showing

signs of DR are further categorized on a scale of 0 (no DR) to 4 (proliferative DR) based on disease severity. In our study, we have taken 1200 fundus images showing normal retina and a collection of 1200 images showing various levels of disease severity, i.e., 300 images each from each severity level 1- 4. Fig. 1(a) and Fig. 1(b) show instances of negative and disease-positive samples in this dataset.

(ii) Shenzhen TB CXR: A set of 326 CXRs showing normal lungs and 336 CXRs showing other Tuberculosis (TB)-related manifestations were collected from the patients at the No.3 hospital in Shenzhen, China. The dataset was de-identified, exempted from IRB review (OHSRP#5357), and released by the National Library of Medicine (NLM). An equal number of 326 CXRs showing normal lungs and TB-related manifestations are used in this study. Fig. 1(c) and Fig. 1(d) show examples from this dataset.

All images are (i) resized to  $256 \times 256$  spatial resolution, (ii) contrast-enhanced using Contrast Limited Adaptive Histogram Equalization (CLAHE) algorithm, and (iii) rescaled to the range [0 1] to improve model stability and performance.

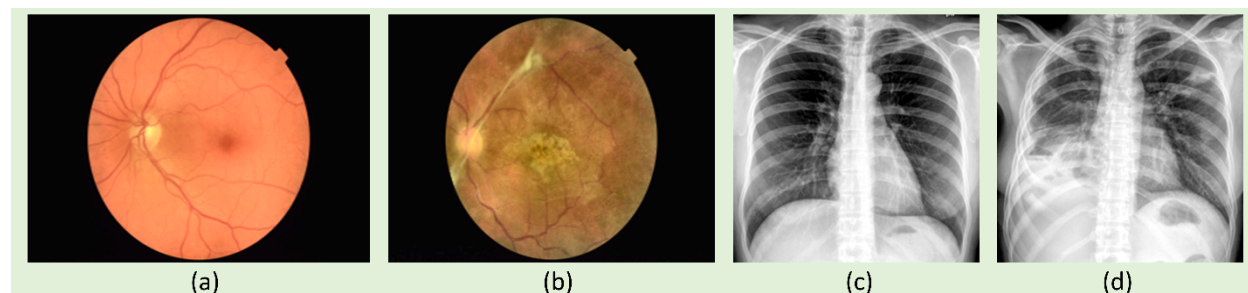


**Fig. 1. Instances of images from various data collections.** (a) and (b) Fundus photographic images showing normal retina and signs of DR, respectively; (c) and (d) CXRs showing normal lungs and TB-related manifestations, respectively.

## 2.2. Simulating imbalance in the training dataset

The datasets are further divided into multiple sets with varying degrees of imbalance of the positive disease samples as shown in Table 1. The number of images in the train and test set for each of these datasets is shown in Table 2. Of the number of training samples in each set, 10% of the data is allocated to validation with a fixed seed.

**Table 1. Dataset notations based on the degree of imbalance of the positive disease samples.**

| Dataset split | Description   |
|---------------|---|
| Set-100       | An equal number of disease-positive and negative samples                  |
| Set-80        | The number of disease-positive samples is 80% of that in the negative set |
| Set-60        | The number of disease-positive samples is 60% of that in the negative set |
| Set-40        | The number of disease-positive samples is 40% of that in the negative set |
| Set-20        | The number of disease-positive samples is 20% of that in the negative set |

**Table 2. Datasets and their respective splits for the data collections used in this study.**

| Data    | Shenzhen TB CXR |     |            |     | APTOS 2019 fundus |      |            |     |
|---------|-----------------|-----|------------|-----|-------------------|------|------------|-----|
|         | Train           |     | Test       |     | Train             |      | Test       |     |
|         | No finding      | TB  | No finding | TB  | No finding        | DR   | No finding | DR  |
| Set-100 | 226             | 226 | 100        | 100 | 1000              | 1000 | 300        | 300 |
| Set-80  | 226             | 180 | 100        | 100 | 1000              | 800  | 300        | 300 |
| Set-60  | 226             | 136 | 100        | 100 | 1000              | 600  | 300        | 300 |
| Set-40  | 226             | 90  | 100        | 100 | 1000              | 400  | 300        | 300 |
| Set-20  | 226             | 45  | 100        | 100 | 1000              | 200  | 300        | 300 |

### 2.3. Classification models

We used three popular and high-performing DL models in this study, namely, VGG-16, DenseNet-121, and Inception-V3. These models have demonstrated superior performance in medical computer vision tasks [1]. They are (i) instantiated with their ImageNet-pretrained weights, (ii) truncated at their deepest convolutional layer, and (iii) appended with a global average pooling (GAP) layer, a final dense layer with two output nodes and softmax activation to normalize models output to a probability distribution over the predicted classes. The models are fine-tuned on the Set-100 dataset from the (i) Shenzhen TB CXR collection and (ii) APTOS 2019 fundus image collection to predict probabilities toward classifying them to their respective categories. Callbacks are used to store model checkpoints. The weights that deliver superior performance with the validation set are further stored and used for predicting the test set. The best-performing model is selected to be finetuned on Set-80, Set-60, Set-40, and Set-20 datasets from (i) Shenzhen TB CXR collection and (ii) APTOS 2019 fundus image collection, and the performances are recorded. The models are retrained using a stochastic gradient descent optimizer with an initial learning rate of  $1e-3$  and momentum of 0.9. The learning rate is reduced whenever the validation loss plateaued. Fig. 2 shows the general block diagram with various dataset inputs to the DL models and their corresponding dataset-specific predictions.

### 2.4. Evaluation:

The following metrics are used to evaluate the models' performance: (a) Accuracy, (b) AUC, (c) Sensitivity/Recall, (d) Precision, (e) F-score, and (f) Matthews correlation coefficient (MCC). We used Tensorflow version 2.4 and CUDA dependencies to train and evaluate the models in a Windows<sup>®</sup> computer with Intel Xeon processor and NVIDIA GeForce GTX 1070 GPU.

### 2.5. Threshold selection:

The evaluation is first carried out using the default classification threshold of 0.5, i.e. predictions  $\geq 0.5$  will be categorized as abnormal (disease-class) and those that are  $< 0.5$  will be categorized as samples showing no findings. However, using a theoretical threshold of 0.5 may adversely impact classification particularly in an imbalanced training scenario [25]. The study in

[26] reveals that it would be misleading to resort to data resampling techniques without trying to find the optimal decision threshold for the task.

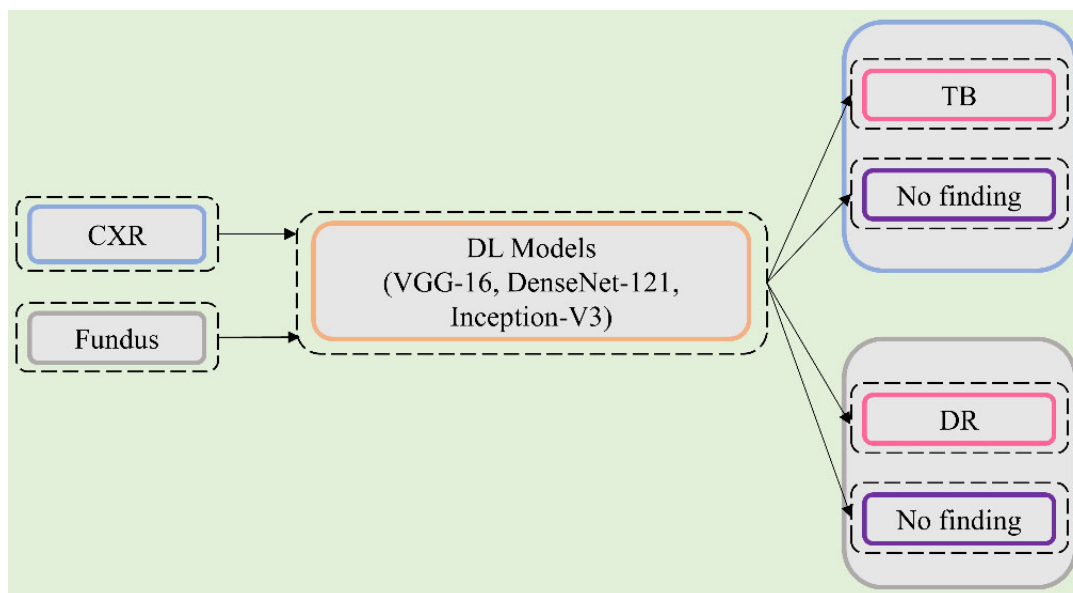


**Fig. 2. Block diagram showing the various dataset inputs to the DL models and their corresponding dataset-specific predictions.**

There are several approaches to finding the optimal threshold for the classification task. These are broadly classified into (i) ROC curve-based methods [27], [28] and (ii) Precision-recall (PR) curve-based methods [29]. In ROC curve-based approach, different values of thresholds are used to interpret the false-positive rate (FPR) and true-positive rate (TPR). The area under the ROC curve (AUROC) summarizes the model performance. A higher value for the AUROC (close to 1.0) signifies superior performance. Metrics such as geometric means (G-means) and Youden statistic ( $J$ ) are evaluated to identify this optimal threshold from ROC curves. The precision and recall values are given by their standard formulae [27], [28]. The optimal threshold results in a superior balance of precision and recall and can be measured using the PR-curve by maximizing the F-score. The value of the F-score is computed for each threshold and its largest value and the corresponding threshold are recorded. This threshold is then used to predict unseen samples and convert the class probabilities to crisp image-level labels. Unlike ROC curves, the PR curves focus on model performance for the positive disease class that is the high-impact event in a classification task. Hence, they are more informative than the ROC curves, particularly in an imbalanced classification task [29].

## 2.6. Calibration

### 2.6.1. Definition of calibration:

The goal of calibration is to find a function that fits the relationship between the predicted probability and the true likelihood of occurrence of the event of interest. Let the output of a DL model  $D$  be denoted by  $h(D) = (X', P')$ , where  $X'$  is the class label obtained from the predicted

probability  $P'$  that needs to be calibrated to reflect the true likelihood of occurrence. If the outputs of the model are perfectly calibrated then,

$$\mathbb{P}(X' = X|P' = p) = p, \forall p \in [0, 1]$$

### 2.6.2. Qualitative evaluation of calibration - Reliability diagram:

The calibration curve or reliability diagram provides a qualitative description of calibration. It is plotted by dividing the predicted probabilities into a fixed number of bins  $Z$ , each of size  $1/Z$ , and having equal width, along the x-axis. Let  $C_z$  denote the set of sample indices whose predicted probabilities fall into the interval  $I_z = (\frac{z-1}{Z}, \frac{z}{Z})$ , for  $z \in \{1, 2, \dots, Z\}$ . The accuracy of the bin  $C_z$  is given by,

$$Accuracy(C_z) = 1/|C_z| \sum_{i \in C_z} 1(y_i' = y_i)$$

The average probability in the bin  $C_z$  is given by:

$$Average\ Probability(C_z) = 1/|C_z| \sum_{i \in C_z} p_i'$$

Here,  $p_i'$  is the probability predicted for the sample  $i$ . With improving calibration, the points will lie closer to the main diagonal that extends from the bottom left to the top right of the reliability diagram. Fig. 3 shows a sample sketch of the reliability diagram. The points below the diagonal indicate that the model is overconfident, and the predicted probabilities are too large. Those above the diagonal indicate that the model is underconfident, and the predicted probabilities are too small.

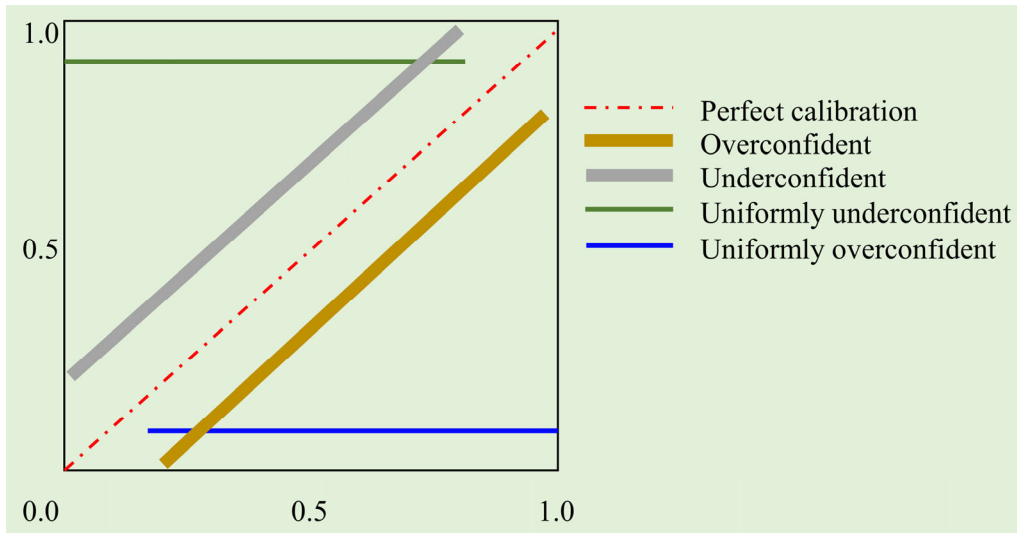


**Fig. 3. A sample sketch of the reliability diagram showing perfectly calibrated, overconfident, underconfident, uniformly overconfident, and uniformly underconfident predictions.**

### 2.6.3. Quantitative evaluation of calibration:

#### 2.6.3.1. Expected calibration error (ECE):

ECE provides a quantitative measure of miscalibration. It is given by the expectation difference between the predicted probabilities and accuracy as shown below:

$$\text{Calibration error} = E_{p'}[\text{abs}((X' = X|P' = p) - p)]$$

In practice, this is computed as the weighted average of the difference between the predicted probabilities and accuracy in each bin.

$$ECE = \sum_{z=1}^z \frac{|C_z|}{m} |\text{accuracy}(C_z) - \text{probability}(C_z)|$$

Here,  $m$  is the total number of samples across all the probability bins. The value of  $ECE = 0$  denotes the model is perfectly calibrated since  $\text{accuracy}(C_z) = \text{probability}(C_z)$  for all bins  $z$ .

#### 2.6.3.2. Log loss:

Log loss captures the extent to which the confidence scores diverge from ground truth class labels. Log loss compares the predicted probability  $p = P_r(y = 1)$  to its true probability  $y \in \{0, 1\}$ . It logarithmically penalizes the predicted probability  $p$  based on its distance from the true probability  $y$  and is given by,

$$L_{\log}(y, p) = -\log P_r(y|p) = -(y \log(p) + (1 - y) \log(1 - p))$$

This results in smaller values of log loss for smaller distances and bigger values for larger distances. The value of log loss is calculated for each predicted probability and the average loss is reported. A model with perfect skill would have a log loss score of 0.0. Log loss analysis is preferred in healthcare applications where the positive disease outcomes are considered rare events and that it would give an arbitrarily high penalty for getting these rare events completely wrong with high confidence.

### 2.6.4. Calibration methods:

The following calibration methods are used in this study: (i) Platt scaling, (ii) beta calibration, and (iii) spline calibration.

#### 2.6.4.1. Platt scaling:

Platt scaling [30] assumes a logistic relationship between the predicted probabilities ( $z$ ) and true probability ( $p$ ). It fits two parameters  $\alpha$  and  $\beta$  and is given by,



$$p = 1/(1 + \exp(-(\alpha + \beta z)))$$

The parameters  $\alpha$  and  $\beta$  are real-valued. The principal benefit of Platt scaling is that it needs very little data since it fits only two parameters. However, the limitation is there is a very restricted set of possible functions. That is, this method will deliver superior calibrated probabilities only if there exists a logistic relationship between  $z$  and  $p$ .

#### 2.6.4.2. Beta calibration:

Literature studies reveal that Platt scaling-based calibration delivers sub-optimal calibrated probabilities even compared to the original uncalibrated scores under circumstances when the classifiers produce heavily skewed score distributions. Under such circumstances, beta calibration [12] methods are shown to deliver superior calibration performance compared to Platt scaling. It is given by,

$$p = \left( 1 + \frac{1}{\exp(c) \frac{z^a}{(1-z)^b}} \right)^{-1}$$

The approach is similar to Platt scaling but with a couple of important improvements. It is a three-parameter family of curves ( $a$ ,  $b$ , and  $c$ ) compared to the 2-parameters as used in Platt scaling. Beta calibration permits the diagonal  $y=x$  as one of the possible functions, so it would not affect an already calibrated classifier.

#### 2.6.4.3. Spline calibration:

Spline calibration [13] is proposed to be a robust, non-parametric calibration method that uses cubic smoothing splines rather than piecewise constant or sigmoid functions to map the uncalibrated scores to true probabilities. Smoothing splines strike a balance between fitting the points well and having a smooth function. It uses a smoothed logistic function, so, the fit to the data is measured by likelihood and the smoothness refers to the integrated second derivative before the logistic transformation. A nuisance parameters trades-off smoothness for fit. It runs a lot of logistic regressions and picks the one with the best nuisance parameter. It transforms the data to provide appropriate scaling for over-confident models.

### 2.7. Statistical analysis:

Statistical analyses are performed to investigate if the performance differences between the models were statistically significant. We used 95% confidence intervals (CI) as the Wilson score interval for the MCC metric to compare the performance of the models trained and evaluated with datasets of varying imbalances. The CI values are also used to observe if there exists a statistically significant difference in the ECE metric before and after calibration. The Python StatsModels module is used to perform these evaluations.

### 3. Results:

#### 3.1. Classification performance achieved with Set-100 dataset:

Recall that VGG-16, DenseNet-121, and Inception-V3 models are fine-tuned on the Set-100 dataset (with no class imbalance) from (i) APTOS 2019 fundus and (ii) Shenzhen TB CXR image collections, to classify them to their respective categories. This approach is followed to select the best-performing model that would subsequently be used to fine-tune the class-imbalance simulated Set-20, Set-40, Set-60, and Set-80 datasets constructed from each of these image collections. Table 3 shows the performance achieved by these models in this regard.

**Table 3. Test performance achieved by the models when fine-tuned on the Set-100 dataset, individually from APTOS 2019 fundus (n=600) and Shenzhen TB CXR (n = 200) image collections.** Data in parenthesis are 95% CI as the Wilson score interval provided for the MCC metric. The best performances are denoted by bold numerical values in the corresponding columns.

| Metric    | Set-100 dataset               |  |                              |   |                               |                               |
|-----------|-------------------------------|--|------------------------------|---|-------------------------------|-------------------------------|
|           | APTOS 2019 fundus             |  |                              | Shenzhen TB CXR                                   |                               |                               |
|           | VGG-16                        | DenseNet-121                                       | Inception-V3                 | VGG-16  | DenseNet-121                  | Inception-V3                  |
| Accuracy  | 0.7983                        | <b>0.8367</b>                                      | 0.8033                       | <b>0.785</b>                                      | 0.7                           | 0.57                          |
| AUROC     | <b>0.9662</b>                 | 0.9168   | 0.8916                       | <b>0.8807</b>                                     | 0.7813                        | 0.6615                        |
| AUPRC     | <b>0.9723</b>                 | 0.929  | 0.9118                       | <b>0.8869</b>                                     | 0.8                           | 0.6215                        |
| Recall    | <b>0.9633</b>                 | 0.84   | 0.8367                       | <b>0.89</b>                                       | 0.49                          | 0.34                          |
| Precision | 0.7243                        | <b>0.8344</b>                                      | 0.7844                       | 0.7355  | <b>0.8448</b>                 | 0.6296                        |
| F-score   | 0.8269                        | <b>0.8372</b>                                      | 0.8097                       | <b>0.8054</b>                                     | 0.6202                        | 0.4416                        |
| MCC       | 0.6321<br>(0.5935,<br>0.6707) | <b>0.6733</b><br><b>(0.6357,</b><br><b>0.7109)</b> | 0.608<br>(0.5689,<br>0.6471) | <b>0.583</b><br><b>(0.5146,</b><br><b>0.6514)</b> | 0.4408<br>(0.3719,<br>0.5097) | 0.1577<br>(0.1071,<br>0.2083) |

Fig. 4 shows the confusion matrix and ROC curves obtained using the DenseNet-121 and VGG-16 models, respectively. It is observed from Table 3 that, when fine-tuned on the Set-100 dataset from the APTOS 2019 fundus image collection, the DenseNet-121 model demonstrated superior performance in terms of accuracy, precision, F-score, and MCC metrics. The VGG-16 model delivered superior values for AUC and recall. The 95% CI for the MCC metric achieved by the DenseNet-121 model demonstrated a tighter error margin, hence, better precision, and is observed to be significantly superior ( $p < 0.05$ ) compared to that achieved with other models. Since the F-score and MCC metric provide a balanced measure of precision and recall, the DenseNet-121 model is selected to be fine-tuned and evaluated on the class-imbalance simulated datasets constructed from the APTOS 2019 fundus image collection. Considering the Shenzhen TB CXR collection, the VGG-16 model delivered superior performance for accuracy, AUC, recall, and F-score and a significantly superior value for the MCC metric ( $p < 0.05$ ) compared to other models. Hence, the VGG-16 model is selected to be fine-tuned and evaluated on the class-imbalance simulated datasets constructed from the Shenzhen TB CXR image collection.

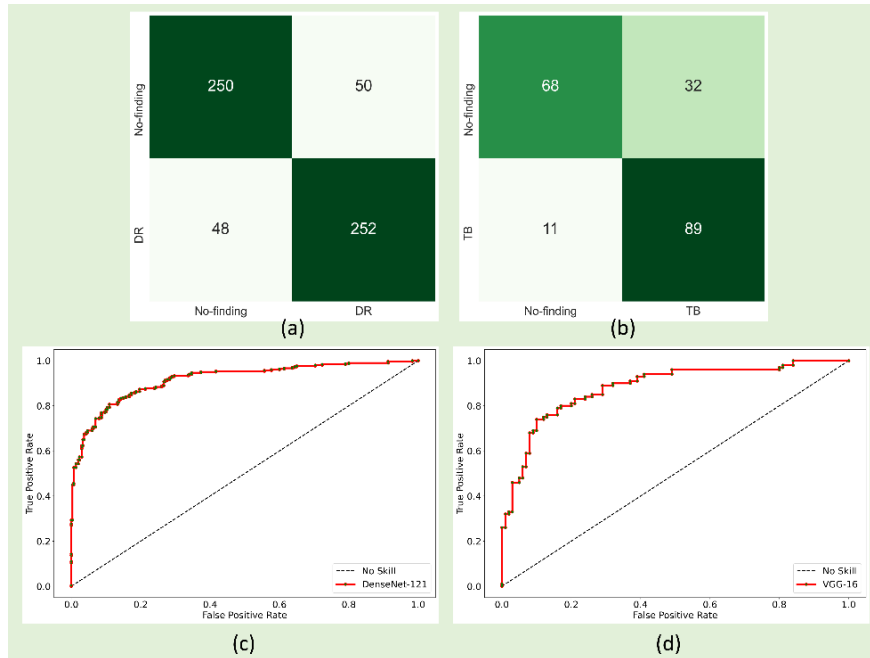


**Fig. 4.** Test performance achieved by the models when fine-tuned and evaluated using the Set-100 dataset. (a) and (b) confusion matrix obtained with the DenseNet-121 and VGG-16 models, respectively, using the APTOS 2019 fundus and Shenzhen TB CXR image collections; (c) and (d) ROC curves obtained with the DenseNet-121 and VGG-16 models, respectively, using the APTOS 2019 fundus and Shenzhen TB CXR image collections.

### 3.2. Classification and calibration performance measurements with class-imbalance simulated datasets:

#### 3.2.1. With APTOS 2019 fundus image collection:

Next, the best-performing DenseNet-121 model is fine-tuned on the class-imbalance simulated datasets. Table 4, Table 5, Table 6, and Table 7 shows the test performance of the model achieved with Set-20, Set-40, Set-60, and Set-80 datasets.

**Table 4.** Test performance achieved by the DenseNet-121 model using the Set-20 dataset constructed from the APTOS 2019 fundus image collection ( $n = 600$ ). Data in parenthesis are 95% CI as the Wilson score interval provided for the MCC and ECE metric. The best performances are denoted by bold numerical values in the corresponding rows. Baseline denotes the model with uncalibrated probabilities. The value  $t_{PR} = 0.5$  denotes the default operating threshold. The last two columns denote the performance achieved with the PR-guided threshold obtained using the uncalibrated and calibrated probabilities, respectively.

| Metric   | Baseline<br>( $t_{PR} = 0.5$ ) | Platt<br>( $t_{PR} = 0.5$ ) | Beta<br>( $t_{PR} = 0.5$ ) | Spline<br>( $t_{PR} = 0.5$ ) | Baseline<br>( $t_{PR-opt} = 0.2143$ ) | Platt<br>( $t_{PR-opt} = 0.4701$ ) |
|----------|--------------------------------|-----------------------------|----------------------------|------------------------------|---------------------------------------|------------------------------------|
| Accuracy | 0.7417                         | 0.8117                      | 0.8117                     | 0.8150                       | <b>0.8133</b>                         | <b>0.8133</b>                      |
| AUROC    | 0.8781                         | 0.8781                      | 0.8781                     | 0.8781                       | <b>0.8781</b>                         | <b>0.8781</b>                      |

|                     |                               |  |                               |                               |                                    |  |
|---------------------|-------------------------------|--|-------------------------------|-------------------------------|------------------------------------|--|
| AUPRC               | 0.9034                        | 0.9034                                 | 0.9034                        | 0.9034                        | <b>0.9034</b>                      | <b>0.9034</b>                          |
| PR-guided threshold | 0.2143                        | 0.4701                                 | 0.4723                        | 0.4587                        | 0.2143                             | 0.4701                                 |
| Precision           | 0.9801                        | 0.8696                                 | 0.8696                        | 0.8795                        | <b>0.8561</b>                      | <b>0.8561</b>                          |
| Recall              | 0.4933                        | 0.7333                                 | 0.7333                        | 0.7300                        | <b>0.7533</b>                      | <b>0.7533</b>                          |
| F-score             | 0.6563                        | 0.7957                                 | 0.7957                        | 0.7978                        | <b>0.8014</b>                      | <b>0.8014</b>                          |
| MCC                 | 0.5569<br>(0.5171,<br>0.5967) | 0.6311 (0.5924,<br>0.6698)             | 0.6311<br>(0.5924,<br>0.6698) | 0.6393 (0.6008,<br>0.6778)    | <b>0.6312 (0.5925,<br/>0.6699)</b> | <b>0.6312<br/>(0.5925,<br/>0.6699)</b> |
| Log loss            | 0.6074                        | 0.4156                                 | <b>0.4130</b>                 | 0.4132                        | 0.6074                             | 0.4156                                 |
| ECE                 | 0.2124<br>(0.1796,<br>0.2452) | <b>0.0327<br/>(0.0184,<br/>0.0470)</b> | 0.0363<br>(0.0213,<br>0.0513) | 0.0454<br>(0.0287,<br>0.0621) | 0.2124<br>(0.1796,<br>0.2452)      | <b>0.0327<br/>(0.0184,<br/>0.0470)</b> |

**Table 5. Test performance achieved by the DenseNet-121 model using the Set-40 dataset constructed from the APTOS 2019 fundus image collection (n = 600).** Data in parenthesis are 95% CI as the Wilson score interval provided for the MCC and ECE metric. The best performances are denoted by bold numerical values in the corresponding rows.

| Metric              | Baseline<br>(tpr = 0.5)       | Platt<br>(tpr = 0.5)          | Beta<br>(tpr = 0.5)           | Spline<br>(tpr = 0.5)                  | Baseline<br>(tpr-opt =<br><b>0.2559</b> ) | Spline<br>(tpr-opt =<br><b>0.4411</b> ) |
|---------------------|-------------------------------|-------------------------------|-------------------------------|--|---|---|
| Accuracy            | 0.8833                        | 0.8917                        | 0.8917                        | 0.8883                                 | <b>0.895</b>                              | <b>0.895</b>                            |
| AUROC               | 0.9617                        | 0.9617                        | 0.9617                        | 0.9617                                 | <b>0.9617</b>                             | <b>0.9617</b>                           |
| AUPRC               | 0.9681                        | 0.9681                        | 0.9681                        | 0.9681                                 | <b>0.9681</b>                             | <b>0.9681</b>                           |
| PR-guided threshold | 0.2559                        | 0.3740                        | 0.4424                        | 0.4411                                 | 0.2559                                    | 0.4411                                  |
| Precision           | 0.9873                        | 0.9273                        | 0.9211                        | 0.9206                                 | <b>0.9129</b>                             | <b>0.9129</b>                           |
| Recall              | 0.7767                        | 0.8500                        | 0.8567                        | 0.8500                                 | <b>0.8733</b>                             | <b>0.8733</b>                           |
| F-score             | 0.8694                        | 0.8870                        | 0.8877                        | 0.8839                                 | <b>0.8927</b>                             | <b>0.8927</b>                           |
| MCC                 | 0.7847<br>(0.7518,<br>0.8176) | 0.7861<br>(0.7532,<br>0.8190) | 0.7853<br>(0.7524,<br>0.8182) | 0.7790<br>(0.7457,<br>0.8123)          | <b>0.7907<br/>(0.7581,<br/>0.8233)</b>    | <b>0.7907<br/>(0.7581,<br/>0.8233)</b>  |
| Log loss            | 0.3089                        | 0.2528                        | 0.2420                        | <b>0.2400</b>                          | 0.3089                                    | <b>0.2400</b>                           |
| ECE                 | 0.0986<br>(0.0747,<br>0.1225) | 0.0464<br>(0.0295,<br>0.0633) | 0.0258<br>(0.0131,<br>0.0385) | <b>0.0194<br/>(0.0083,<br/>0.0325)</b> | 0.0986<br>(0.0747,<br>0.1225)             | <b>0.0194<br/>(0.0083,<br/>0.0325)</b>  |

**Table 6. Test performance achieved by the DenseNet-121 model using the Set-60 dataset constructed from the APTOS 2019 fundus image collection (n = 600).** Data in parenthesis are 95% CI as the Wilson score interval provided for the ECE metric. The best performances are denoted by bold numerical values in the corresponding rows.

| Metric | Baseline | Platt | Beta | Spline | Baseline | Platt |
|--------|----------|-------|------|--------|----------|-------|
|--------|----------|-------|------|--------|----------|-------|

|                     | (tpr = 0.5)                   | (tpr = 0.5)                                       | (tpr = 0.5)                   | (tpr = 0.5)                   | (tpr-opt = 0.3577)                                 | (tpr-opt = 0.5339)                                 |
|---------------------|-------------------------------|---|-------------------------------|-------------------------------|--|--|
| Accuracy            | 0.8500                        | 0.8600  | 0.8700                        | 0.8600                        | <b>0.8683</b>                                      | <b>0.8683</b>                                      |
| AUROC               | 0.9312                        | 0.9312  | 0.9312                        | 0.9312                        | <b>0.9312</b>                                      | <b>0.9312</b>                                      |
| AUPRC               | 0.9455                        | 0.9455  | 0.9455                        | 0.9455                        | <b>0.9455</b>                                      | <b>0.9455</b>                                      |
| PR-guided threshold | 0.3577                        | 0.5339  | 0.5007                        | 0.4587                        | 0.3577   | 0.5339   |
| Precision           | 0.9646                        | 0.8885  | 0.9111                        | 0.9186                        | <b>0.9108</b>                                      | <b>0.9108</b>                                      |
| Recall              | 0.7267                        | 0.8233  | 0.8200                        | 0.7900                        | <b>0.8167</b>                                      | <b>0.8167</b>                                      |
| F-score             | 0.8289                        | 0.8789  | 0.8632                        | 0.8495                        | <b>0.8612</b>                                      | <b>0.8612</b>                                      |
| MCC                 | 0.7223<br>(0.6864,<br>0.7582) | 0.7219<br>(0.6860,<br>0.7578)                     | 0.7437<br>(0.7087,<br>0.7787) | 0.7272<br>(0.6915,<br>0.7629) | <b>0.7406</b><br><b>(0.7055,</b><br><b>0.7757)</b> | <b>0.7406</b><br><b>(0.7055,</b><br><b>0.7757)</b> |
| Log loss            | 0.3886                        | 0.3208  | 0.3143                        | <b>0.3105</b>                 | 0.3886   | 0.3208   |
| ECE                 | 0.1063<br>(0.0816,<br>0.131)  | <b>0.0409</b><br><b>(0.025,</b><br><b>0.0568)</b> | 0.0435<br>(0.0271,<br>0.0599) | 0.0439<br>(0.0275,<br>0.0603) | 0.1063<br>(0.0816,<br>0.131)                       | <b>0.0409</b><br><b>(0.025,</b><br><b>0.0568)</b>  |

**Table 7. Test performance achieved by the DenseNet-121 model using the Set-80 dataset constructed from the APTOS 2019 fundus image collection (n = 600).** Data in parenthesis are 95% CI as the Wilson score interval provided for the MCC and ECE metric. The best performances are denoted by bold numerical values in the corresponding rows.

| Metric              | Baseline (tpr = 0.5)          | Platt (tpr = 0.5)             | Beta (tpr = 0.5)              | Spline (tpr = 0.5)                                 | Baseline (tpr-opt = 0.3211)                        | Spline (tpr-opt = 0.3279)                          |
|---------------------|-------------------------------|-------------------------------|-------------------------------|--|--|--|
| Accuracy            | 0.8250                        | 0.8167                        | 0.8267                        | 0.8250   | <b>0.8167</b>                                      | <b>0.8167</b>                                      |
| AUROC               | 0.9017                        | 0.9017                        | 0.9017                        | 0.9017   | <b>0.9017</b>                                      | <b>0.9017</b>                                      |
| AUPRC               | 0.9208                        | 0.9208                        | 0.9208                        | 0.9208   | <b>0.9208</b>                                      | <b>0.9208</b>                                      |
| PR-guided threshold | 0.3211                        | 0.3394                        | 0.3185                        | 0.3279   | 0.3211   | 0.3279   |
| Precision           | 0.8884                        | 0.8393                        | 0.8712                        | 0.8764   | <b>0.795</b>                                       | <b>0.795</b>                                       |
| Recall              | 0.7433                        | 0.7833                        | 0.7667                        | 0.7567   | <b>0.8533</b>                                      | <b>0.8533</b>                                      |
| F-score             | 0.8094                        | 0.8103                        | 0.8156                        | 0.8122   | <b>0.8231</b>                                      | <b>0.8231</b>                                      |
| MCC                 | 0.6588<br>(0.6208,<br>0.6968) | 0.6347<br>(0.5961,<br>0.6733) | 0.6581<br>(0.6201,<br>0.6961) | 0.6562<br>(0.6181,<br>0.6943)                      | <b>0.6350</b><br><b>(0.5964,</b><br><b>0.6736)</b> | <b>0.6350</b><br><b>(0.5964,</b><br><b>0.6736)</b> |
| Log loss            | 0.4118                        | 0.3887                        | 0.3811                        | <b>0.3808</b>                                      | 0.4118   | <b>0.3808</b>                                      |
| ECE                 | 0.0648<br>(0.0451,<br>0.0845) | 0.0402<br>(0.0244,<br>0.056)  | 0.0381<br>(0.0227,<br>0.0535) | <b>0.0331</b><br><b>(0.0187,</b><br><b>0.0475)</b> | 0.0648<br>(0.0451,<br>0.0845)                      | <b>0.0331</b><br><b>(0.0187,</b><br><b>0.0475)</b> |

From the above Tables, we observe that no single calibration method delivered superior performance across all the datasets. Table 4 shows that, with the Set-20 dataset, at the default classification threshold of 0.5, the MCC metric obtained with Platt-scaled probabilities is significantly superior ( $p < 0.05$ ) compared to that obtained with the uncalibrated probabilities. As well, Platt scaling demonstrated the least ECE metric compared to other calibration methods. No statistically significant difference is observed in the ECE values obtained across the calibration methods. In addition to finding performance at the default threshold of 0.5, we also applied the optimal threshold obtained from PR-curve to measure performance. This performance for the calibrated model is, however, not significantly superior ( $p > 0.05$ ) compared to that of the uncalibrated model. Fig. 5 shows the PR curves with their optimal thresholds obtained using the uncalibrated and calibrated probabilities for Set-20, Set-40, Set-60, and Set-80 collections, respectively.

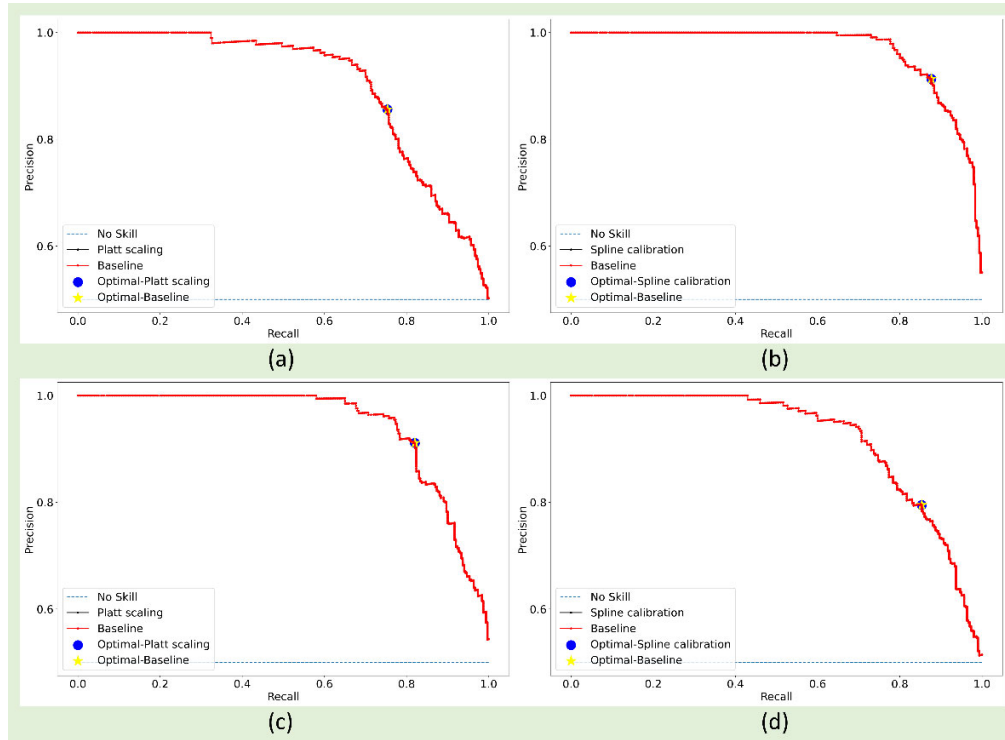


**Fig. 5. PR curves with their optimal thresholds obtained using the uncalibrated and calibrated probabilities for various datasets. (a) Set-20; (b) Set-40; (c) Set-60; and (d) Set-80.**

A similar performance is observed with the Set-40, Set-60, and Set-80 datasets. With Set-40 and Set-80 datasets, spline calibrated probabilities demonstrated the least ECE metric compared to other calibration methods and the baseline uncalibrated model. The 95% CI for the ECE metric for Set-40 and Set-80 datasets using spline calibration demonstrated a tighter error margin and is observed to be significantly smaller ( $p < 0.05$ ) compared to the uncalibrated model. However, we observed no statistically significant difference in the ECE metric obtained across the calibration methods for Set-40, Set-60, and Set-80 datasets. Similar to our observation from Table 4, at the

default operating threshold of 0.5, the MCC metric obtained with spline calibrated probabilities using Set-40 and Set-80 datasets and the Platt-scaled probabilities using Set-60 dataset are significantly superior ( $p < 0.05$ ) compared to that obtained with the baseline, uncalibrated model. However, we observed that the classification performance obtained with the PR-guided threshold using the spline calibrated probabilities for Set-40 and Set-80 datasets and Platt scaling-guided probabilities for the Set-60 dataset are not significantly superior ( $p > 0.05$ ) compared to that obtained using the uncalibrated probabilities. As well, the PR-guided threshold values obtained using Set-20, Set-40, Set-60, and Set-80 datasets are found to be significantly different ( $p < 0.05$ ) for the uncalibrated and calibrated probabilities. Fig. 6 shows the reliability diagrams with their corresponding ECE metrics obtained using the uncalibrated and calibrated probabilities for Set-20, Set-40, Set-60, and Set-80 datasets, respectively.

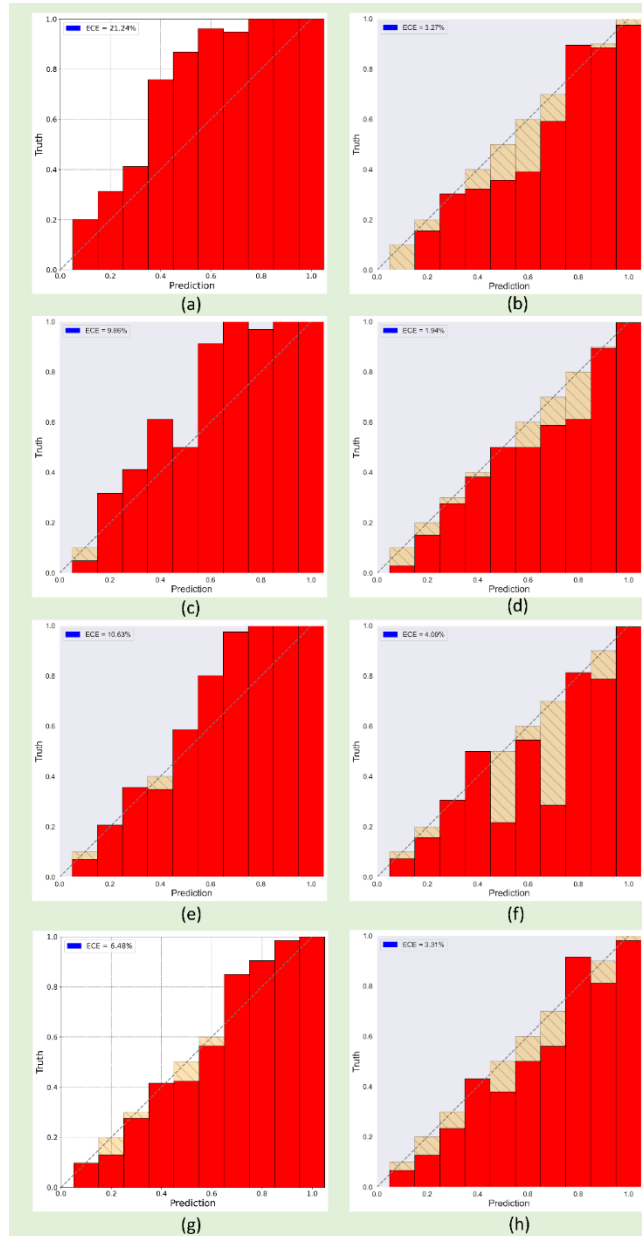


**Fig. 6. Reliability diagrams with their corresponding ECE metrics obtained using the uncalibrated and calibrated probabilities for Set-20, Set-40, Set-60, and Set-80 datasets, respectively.** Calibration errors are shown in yellow. In the figure (a) Set-20-baseline; (b) Set-20-Platt scaling; (c) Set-40-baseline; (d) Set-40-Spline calibration; (e) Set-60-baseline; (f) Set-60-Platt scaling; (g) Set-80-baseline; (h) Set-80-Spline calibration. Average ECE is shown in blue on the top left corner.

As observed from the reliability diagrams in Fig. 6, the models are underconfident about their predictions for Set-20, Set-40, Set-60, and Set-80 datasets since all the points were observed to lie above the diagonal line. However, the calibration methods attempted to map these uncalibrated probabilities to their true occurrence likelihood and bring the points closer to the 45-degree line. Fig. 7 shows the confusion matrices obtained using the uncalibrated and calibrated probabilities at their default and PR-guided thresholds using the Set-20, Set-40, Set-60, and Set-80 datasets, respectively.

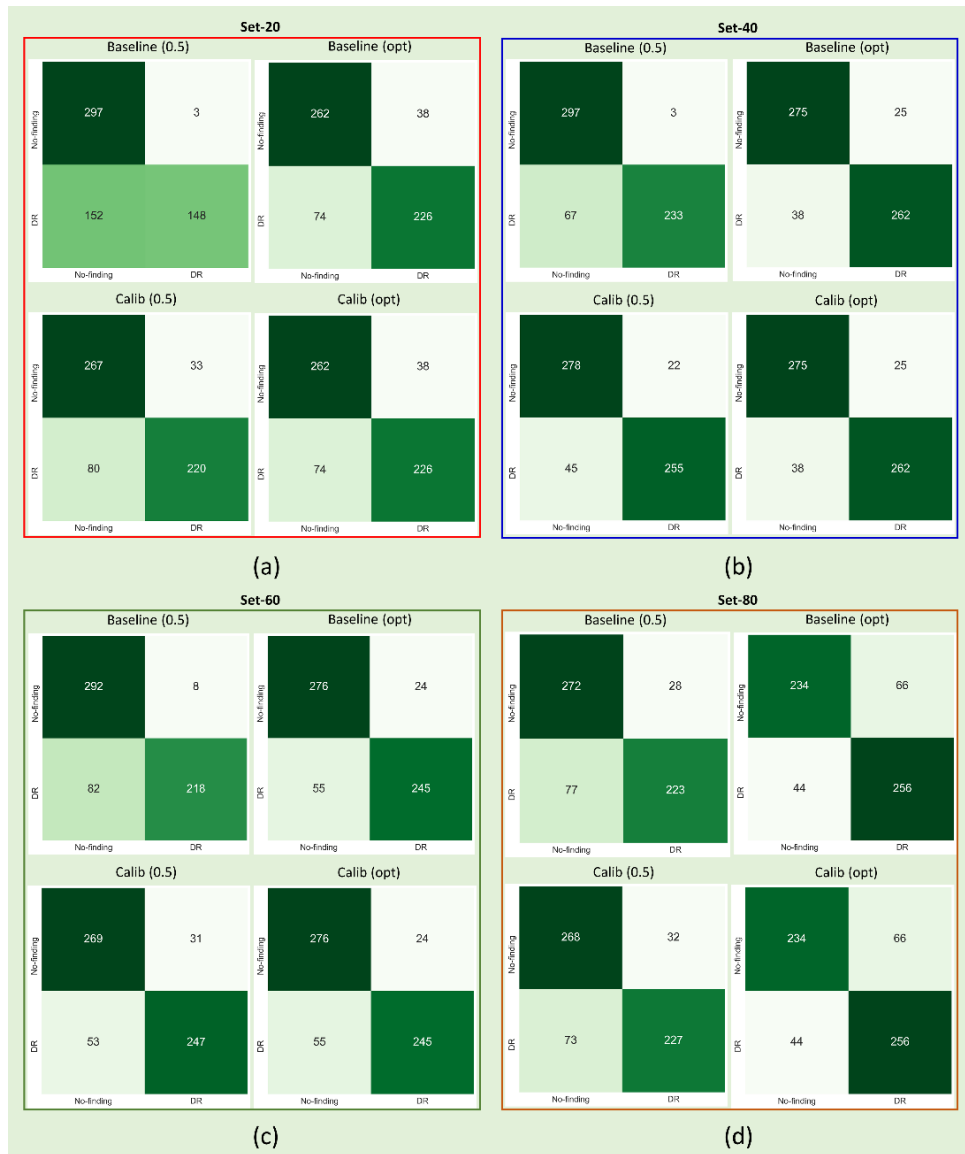




**Fig. 7. Confusion matrices obtained with the uncalibrated and calibrated probabilities (from left to right) for (a) Set-20 dataset : Baseline ( $t_{PR} = 0.5$ ), Baseline ( $t_{PR-opt} = 0.2143$ ), Platt scaling ( $t_{PR} = 0.5$ ), and Platt scaling ( $t_{PR-opt} = 0.4701$ ), respectively; (b) Set-40 dataset: Baseline ( $t_{PR} = 0.5$ ), Baseline ( $t_{PR-opt} = 0.2559$ ), Spline calibration ( $t_{PR} = 0.5$ ), and Spline calibration ( $t_{PR-opt} = 0.4411$ ), respectively; (c) Set-60 dataset: Baseline ( $t_{PR} = 0.5$ ), Baseline ( $t_{PR-opt} = 0.3577$ ), Platt scaling ( $t_{PR} = 0.5$ ), and Platt scaling ( $t_{PR-opt} = 0.5339$ ), respectively; (d) Set-80 dataset: Baseline ( $t_{PR} = 0.5$ ), Baseline ( $t_{PR-opt} = 0.3211$ ), Spline calibration ( $t_{PR} = 0.5$ ), and Spline calibration ( $t_{PR-opt} = 0.3279$ ), respectively.**

From Fig. 7, we observed the following: At the default operating threshold of 0.5, the performance obtained with the calibrated probabilities for Set-20, Set-40, Set-60, and Set-80 datasets is significantly superior ( $p < 0.05$ ) compared to that obtained with the uncalibrated probabilities. The calibrated probabilities resulted in a superior recall and significantly superior ( $p < 0.05$ ) MCC values compared to the baseline, uncalibrated model. This underscores the fact that calibration helped to significantly improve classification performance at the default operating threshold of 0.5. However, at the PR-guided threshold, the classification performance obtained with the calibrated probabilities is not significantly superior ( $p > 0.05$ ) compared to that obtained with the uncalibrated probabilities. However, the PR-guided threshold values derived from the uncalibrated and calibrated probabilities are observed to be significantly different ( $p < 0.05$ ).

### 3.2.2. With Shenzhen TB CXR image collection:

The best-performing VGG-16 model is selected to be subsequently finetuned on Set-20, Set-40, Set-60, and Set-80 datasets. Table 8, Table 9, Table 10, and Table 11 show the test performance achieved with the VGG-16 model using these datasets constructed from the Shenzhen TB CXR collection.

**Table 8. Test performance achieved by the VGG-16 model using the Set-20 dataset ( $n = 200$ ). Data in parenthesis are 95% CI as the Wilson score interval provided for the MCC and ECE metric. The best performances are denoted by bold numerical values in the corresponding rows. Baseline denotes the uncalibrated model. The value  $t_{PR} = 0.5$  denotes the default operating threshold. The last two columns denote the performance achieved using the uncalibrated and calibrated probabilities at their PR-guided thresholds.**

| Metric                 | Baseline<br>( $t_{PR} = 0.5$ ) | Platt<br>( $t_{PR} = 0.5$ ) | Beta<br>( $t_{PR} = 0.5$ ) | Spline<br>( $t_{PR} = 0.5$ ) | Baseline<br>( $t_{PR-opt} = 0.1632$ ) | Spline<br>( $t_{PR-opt} = 0.4192$ ) |
|------------------------|--------------------------------|-----------------------------|----------------------------|------------------------------|---------------------------------------|-------------------------------------|
| Accuracy               | 0.5000                         | 0.6400                      | 0.6400                     | 0.6050                       | 0.6350                                | <b>0.6400</b>                       |
| AUROC                  | 0.6615                         | 0.6615                      | 0.6615                     | 0.6615                       | <b>0.6615</b>                         | <b>0.6615</b>                       |
| AUPRC                  | 0.6494                         | 0.6494                      | 0.6494                     | 0.6494                       | <b>0.6494</b>                         | <b>0.6494</b>                       |
| PR-guided<br>threshold | 0.1632                         | 0.3998                      | 0.4001                     | 0.4192                       | 0.1632                                | 0.4192                              |
| Precision              | N/A                            | 0.6522                      | 0.6489                     | 0.6296                       | 0.5918                                | <b>0.5946</b>                       |
| Recall                 | 0                              | 0.6000                      | 0.6100                     | 0.5100                       | 0.8700                                | <b>0.8800</b>                       |
| F-score                | N/A                            | 0.6250                      | 0.6288                     | 0.5635                       | 0.7044                                | <b>0.7097</b>                       |

|          |                               |                               |                               |  |                               |  |
|----------|-------------------------------|-------------------------------|-------------------------------|--|-------------------------------|--|
| MCC      | N/A                           | 0.2805<br>(0.2182,<br>0.3428) | 0.2809<br>(0.2186,<br>0.3432) | 0.2139<br>(0.1570,<br>0.2708)                      | 0.3059<br>(0.2420,<br>0.3698) | <b>0.3192</b><br><b>(0.2545,</b><br><b>0.3839)</b> |
| Log loss | 0.9502                        | 0.6544                        | 0.6537                        | 0.6583   | 0.9502                        | <b>0.6583</b>                                      |
| ECE      | 0.3237<br>(0.2588,<br>0.3886) | 0.0832<br>(0.0449,<br>0.1215) | 0.1021<br>(0.0601,<br>0.1441) | <b>0.0787</b><br><b>(0.0413,</b><br><b>0.1161)</b> | 0.3237<br>(0.2588,<br>0.3886) | <b>0.0787</b><br><b>(0.0413,</b><br><b>0.1161)</b> |

**Table 9.** Test performance achieved by the VGG-16 model using the Set-40 dataset (n = 200) constructed from the Shenzhen TB CXR image collection.

| Metric                 | Baseline<br>(tpr = 0.5)      | Platt<br>(tpr = 0.5)          | Beta<br>(tpr = 0.5)                                | Spline<br>(tpr = 0.5)         | Baseline<br>(tpr-opt =<br><b>0.2776</b> ) | Beta<br>(tpr-opt =<br><b>0.3458</b> )              |
|------------------------|------------------------------|-------------------------------|--|-------------------------------|---|--|
| Accuracy               | 0.5000                       | 0.7750                        | 0.7700   | 0.7800                        | 0.7900                                    | <b>0.7950</b>                                      |
| AUROC                  | 0.8602                       | 0.8602                        | 0.8602   | 0.8602                        | <b>0.8602</b>                             | <b>0.8602</b>                                      |
| AUPRC                  | 0.8468                       | 0.8468                        | 0.8468   | 0.8468                        | <b>0.8468</b>                             | <b>0.8468</b>                                      |
| PR-guided<br>threshold | 0.2776                       | 0.3374                        | 0.3458   | 0.38528                       | 0.2776                                    | 0.3458   |
| Precision              | N/A                          | 0.7670                        | 0.7596   | 0.7456                        | 0.7377                                    | <b>0.7398</b>                                      |
| Recall                 | 0                            | 0.7900                        | 0.7900   | 0.8500                        | 0.9000                                    | <b>0.9100</b>                                      |
| F-score                | N/A                          | 0.7783                        | 0.7745   | 0.7944                        | 0.8108                                    | <b>0.8161</b>                                      |
| MCC                    | N/A                          | 0.5502<br>(0.4812,<br>0.6192) | 0.5404<br>(0.4713,<br>0.6095)                      | 0.5656<br>(0.4969,<br>0.6343) | 0.5946<br>(0.5265,<br>0.6627)             | <b>0.6063</b><br><b>(0.5385,</b><br><b>0.6741)</b> |
| Log loss               | 0.7415                       | 0.4635                        | 0.4610   | 0.4548                        | 0.7415                                    | <b>0.4610</b>                                      |
| ECE                    | 0.2094<br>(0.153,<br>0.2658) | 0.0628<br>(0.0291,<br>0.0965) | <b>0.0565</b><br><b>(0.0245,</b><br><b>0.0885)</b> | 0.0570<br>(0.0248,<br>0.0892) | 0.2094<br>(0.153,<br>0.2658)              | <b>0.0565</b><br><b>(0.0245,</b><br><b>0.0885)</b> |

**Table 10.** Test performance achieved by the VGG-16 model using the Set-60 dataset (n = 200) constructed from the Shenzhen TB CXR image collection.

| Metric                 | Baseline<br>(tpr = 0.5) | Platt<br>(tpr = 0.5) | Beta<br>(tpr = 0.5) | Spline<br>(tpr = 0.5) | Baseline<br>(tpr-opt =<br><b>0.5177</b> ) | Beta<br>(tpr-opt =<br><b>0.3505</b> ) |
|------------------------|-------------------------|----------------------|---------------------|-----------------------|---|---------------------------------------|
| Accuracy               | 0.7950                  | 0.8050               | 0.8050              | 0.8150                | <b>0.8200</b>                             | 0.8150                                |
| AUROC                  | 0.9004                  | 0.9004               | 0.9004              | 0.9004                | <b>0.9004</b>                             | <b>0.9004</b>                         |
| AUPRC                  | 0.9091                  | 0.9091               | 0.9091              | 0.9091                | <b>0.9091</b>                             | <b>0.9091</b>                         |
| PR-guided<br>threshold | 0.5177                  | 0.4046               | 0.3505              | 0.3548                | 0.5177                                    | 0.3505                                |
| Precision              | 0.7565                  | 0.7905               | 0.8081              | 0.8316                | <b>0.7909</b>                             | 0.7890                                |
| Recall                 | 0.8700                  | 0.8300               | 0.800               | 0.7900                | <b>0.8700</b>                             | 0.8600                                |

|          |                               |                               |  |                               |  |  |
|----------|-------------------------------|-------------------------------|--|-------------------------------|--|--|
| F-score  | 0.8093                        | 0.8098                        | 0.804  | 0.8103                        | <b>0.8286</b>                                      | 0.8230   |
| MCC      | 0.5968<br>(0.5288,<br>0.6648) | 0.6108<br>(0.5432,<br>0.6784) | 0.6100<br>(0.5424,<br>0.6776)                      | 0.6308<br>(0.5639,<br>0.6977) | <b>0.6432</b><br><b>(0.5768,</b><br><b>0.7096)</b> | 0.6326<br>(0.5657,<br>0.6995)                      |
| Log loss | 0.4371                        | 0.4086                        | 0.3979   | 0.3973                        | 0.4371   | <b>0.3979</b>                                      |
| ECE      | 0.0977<br>(0.0565,<br>0.1389) | 0.0645<br>(0.0304,<br>0.0986) | <b>0.0451</b><br><b>(0.0163,</b><br><b>0.0739)</b> | 0.0518<br>(0.021,<br>0.0826)  | 0.0977<br>(0.0565,<br>0.1389)                      | <b>0.0451</b><br><b>(0.0163,</b><br><b>0.0739)</b> |

**Table 11. Test performance achieved by the VGG-16 model using the Set-80 dataset (n = 200) constructed from the Shenzhen TB CXR image collection.**

| Metric                 | Baseline<br>(tpr = 0.5)       | Platt<br>(tpr = 0.5)          | Beta<br>(tpr = 0.5)                                | Spline<br>(tpr = 0.5)         | Baseline<br>(tpr-opt =<br><b>0.6338</b> ) | Beta<br>(tpr-opt =<br><b>0.3753</b> )              |
|------------------------|-------------------------------|-------------------------------|--|-------------------------------|---|--|
| Accuracy               | 0.7550                        | 0.8100                        | 0.8100   | 0.8200                        | 0.8150                                    | <b>0.8200</b>                                      |
| AUROC                  | 0.8936                        | 0.8936                        | 0.8936   | 0.8936                        | <b>0.8936</b>                             | <b>0.8936</b>                                      |
| AUPRC                  | 0.9069                        | 0.9069                        | 0.9069   | 0.9069                        | <b>0.9069</b>                             | <b>0.9069</b>                                      |
| PR-guided<br>threshold | 0.6338                        | 0.4891                        | 0.3753   | 0.3781                        | 0.6338                                    | 0.3753   |
| Precision              | 0.6977                        | 0.7925                        | 0.8229   | 0.8478                        | 0.7944                                    | <b>0.7963</b>                                      |
| Recall                 | 0.9000                        | 0.8400                        | 0.7900   | 0.7800                        | 0.8500                                    | <b>0.8600</b>                                      |
| F-score                | 0.7860                        | 0.8156                        | 0.8061   | 0.8125                        | 0.8213                                    | <b>0.8269</b>                                      |
| MCC                    | 0.5329<br>(0.4637,<br>0.6021) | 0.6211<br>(0.5538,<br>0.6884) | 0.6205<br>(0.5532,<br>0.6878)                      | 0.6421<br>(0.5756,<br>0.7086) | 0.6315<br>(0.5646,<br>0.6984)             | <b>0.6421</b><br><b>(0.5756,</b><br><b>0.7086)</b> |
| Log loss               | 0.4669                        | 0.4279                        | 0.4054   | 0.4062                        | 0.4669                                    | <b>0.4054</b>                                      |
| ECE                    | 0.1326<br>(0.0855,<br>0.1797) | 0.0657<br>(0.0313,<br>0.1001) | <b>0.0363</b><br><b>(0.0103,</b><br><b>0.0623)</b> | 0.0401<br>(0.0129,<br>0.0673) | 0.1326<br>(0.0855,<br>0.1797)             | <b>0.0363</b><br><b>(0.0103,</b><br><b>0.0623)</b> |

Similar to our observation with the APTOS 2019 fundus image collection, no single calibration method delivered superior calibration performance across the class-imbalance simulated datasets constructed from the Shenzhen TB CXR collection. It is observed from Table 8 that, with the Set-20 dataset, at the default threshold of 0.5, the spline calibrated probabilities demonstrated the least values for the ECE metric compared to other calibration methods. The 95% CI for the ECE metric obtained through spline calibration demonstrated a tighter error margin and is significantly smaller ( $p < 0.05$ ) compared to that obtained with uncalibrated probabilities. However, we observed no statistically significant difference in the ECE metric across the calibration methods. We also observed that the MCC metric obtained with spline-calibrated probabilities is significantly superior ( $p < 0.05$ ) compared to that obtained with the uncalibrated model. However, the classification performance obtained with the PR-guided threshold using the spline calibrated probabilities is only marginally but not significantly superior ( $p > 0.05$ ) compared

to that obtained with the PR-guided threshold derived from uncalibrated probabilities. On the other hand, these PR-guided thresholds obtained from spline calibrated and uncalibrated probabilities are observed to be significantly different ( $p < 0.05$ ). A similar pattern of results is observed with the Set-40, Set-60, and Set-80 datasets, respectively, as shown in Table 9, Table 10, and Table 11. The beta calibration method demonstrated the least values for the ECE metric for the Set-40, Set-60, and Set-80 datasets, compared to other calibration methods, and the baseline uncalibrated model. The 95% CI for the ECE metric obtained with beta calibration across Set-40, Set-60, and Set-80 datasets demonstrated higher precision with a tighter error margin and is significantly smaller ( $p < 0.05$ ) compared to that obtained with the uncalibrated probabilities. However, no statistically significant difference in the ECE metric is observed ( $p > 0.05$ ) across the calibration methods. Fig. 8 shows the PR curves with their optimal thresholds obtained using the uncalibrated and calibrated probabilities for Set-20, Set-40, Set-60, and Set-80 collections, respectively.

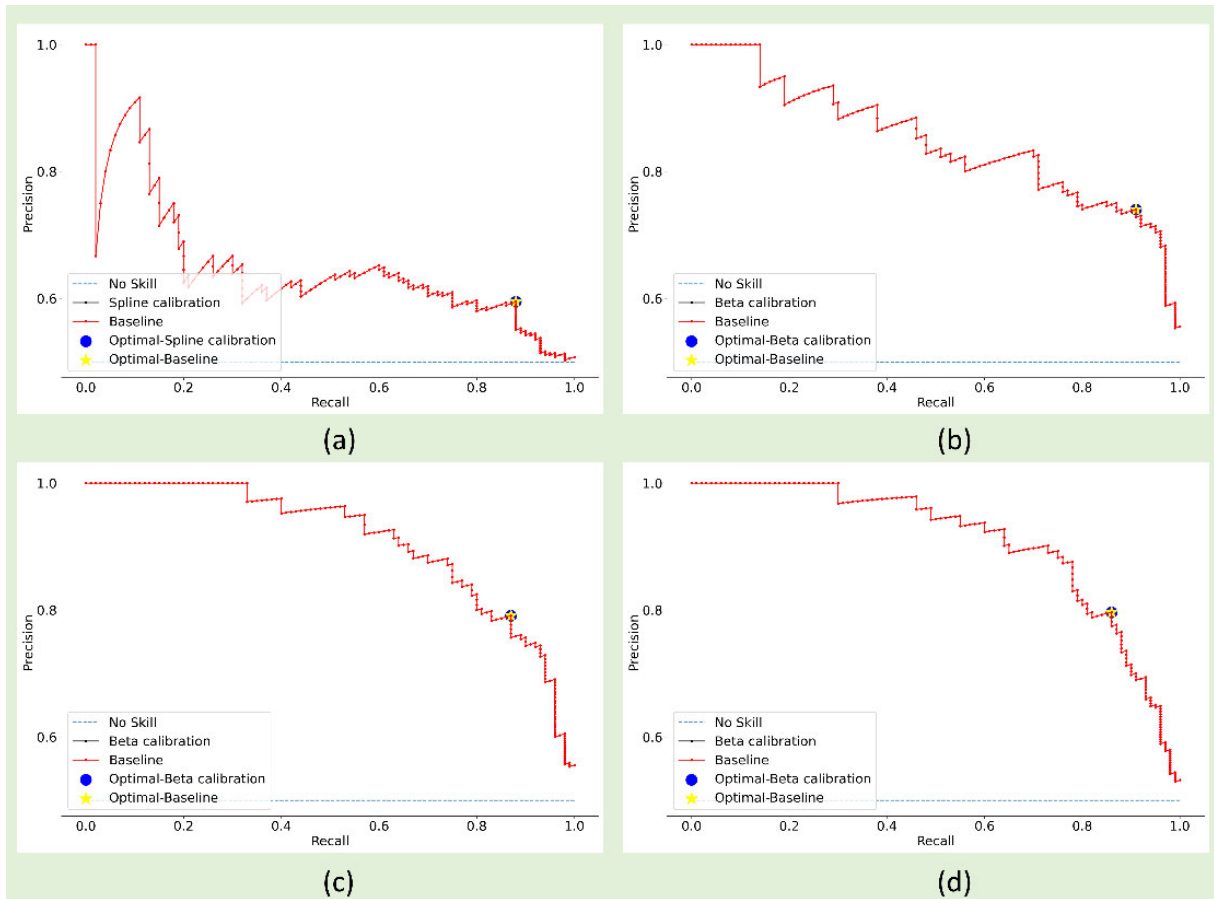


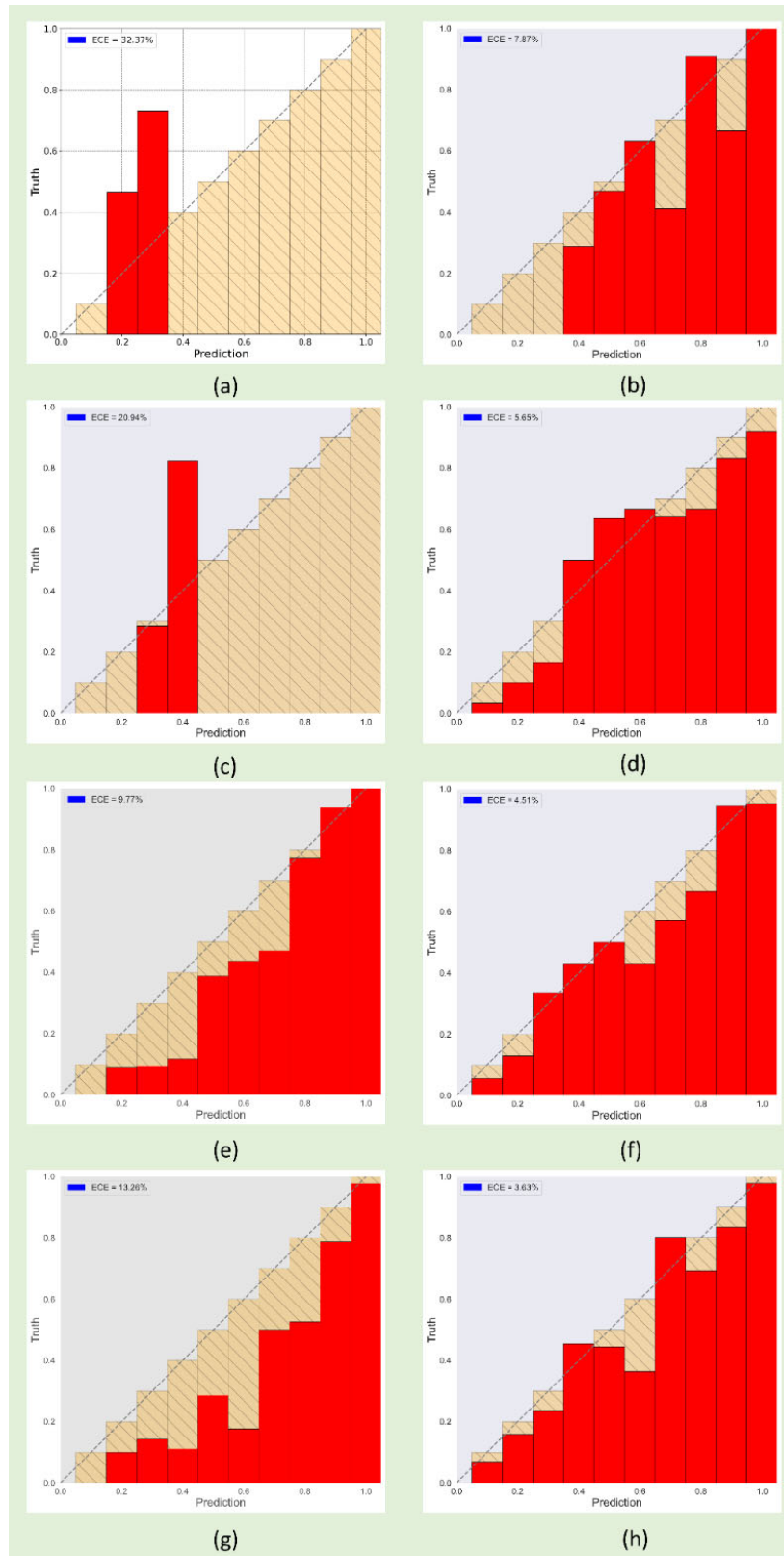
**Fig. 8. PR curves with their optimal thresholds obtained using the uncalibrated and calibrated probabilities for the class-imbalance simulated datasets. (a) Set-20; (b) Set-40; (c) Set-60; and (d) Set-80.**

Similar to our observation from Table 8, we observed from Table 9, Table 10, and Table 11 that, at the default operating threshold of 0.5, the MCC metric obtained with beta calibrated probabilities is significantly superior ( $p < 0.05$ ) compared to the uncalibrated model. From Table

9 and Table 11, we observed that the classification performance obtained with PR-guided threshold derived from beta calibrated probabilities for the Set-40 and Set-80 datasets, respectively, are marginally but not significantly superior ( $p > 0.05$ ) compared to that obtained with the PR-guided threshold derived from uncalibrated probabilities. However, for the Set-60 dataset, as observed from Table 10, the performance obtained using the PR-guided threshold using uncalibrated probabilities is marginally but not significantly superior ( $p > 0.05$ ) compared to that obtained with the beta calibrated probabilities. Across the datasets, we observed that the PR-guided thresholds obtained from spline calibrated and uncalibrated probabilities are observed to be significantly different ( $p < 0.05$ ).

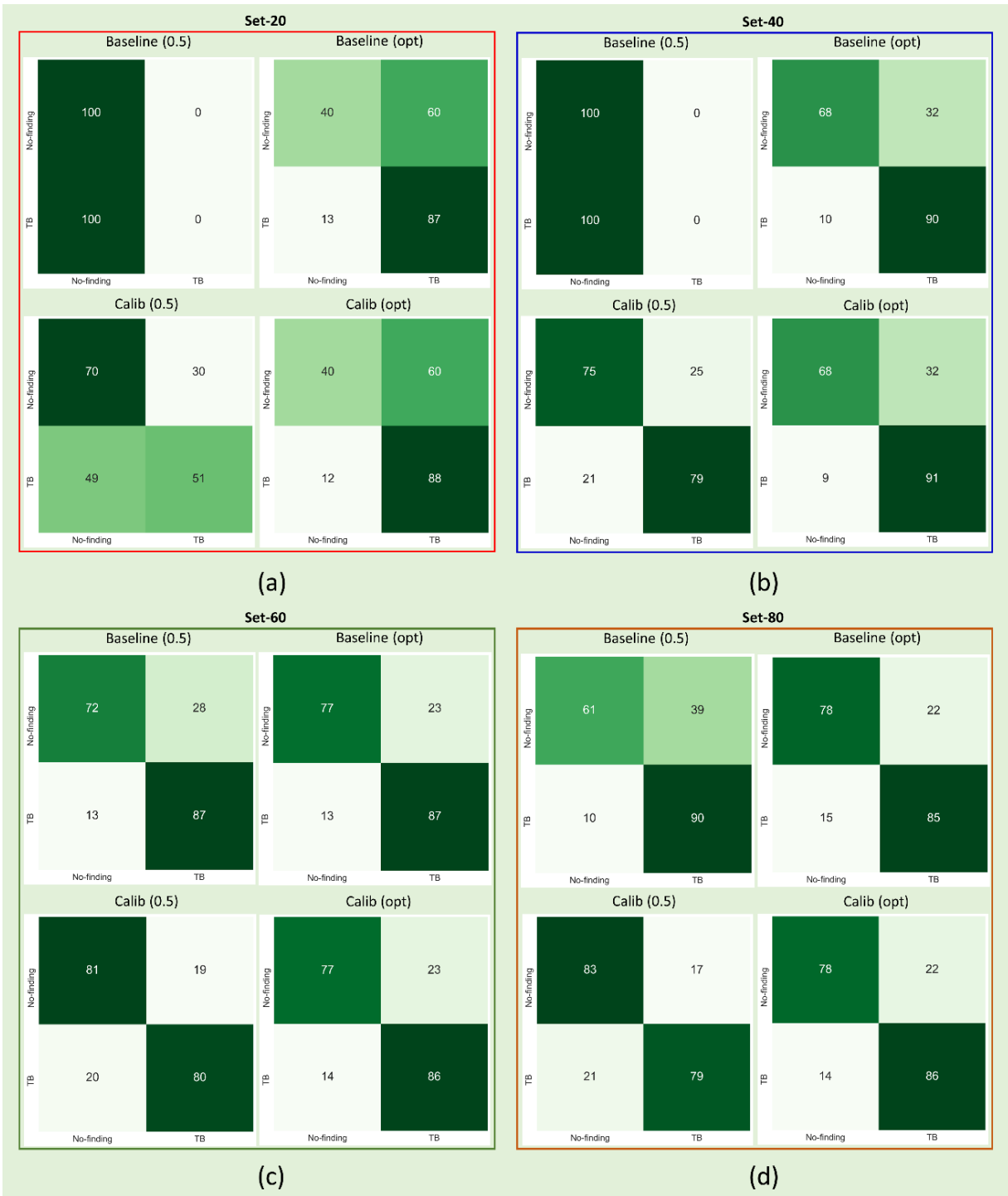
Fig. 9 shows the reliability diagrams with their corresponding ECE metrics obtained using the uncalibrated and calibrated probabilities for Set-20, Set-40, Set-60, and Set-80 datasets, respectively, constructed from the Shenzhen TB CXR image collection. We observed that the model is overly underconfident about its predictions for the Set-20 and Set-40 datasets since all points were found to be lying high above the diagonal line. With Set-60 and Set-80 datasets, the model is observed to be both underconfident and overconfident about its predictions, where the points were found to be lying both above and below the diagonal line. However, the calibration methods attempted to rescale and map these uncalibrated probabilities the true occurrence likelihood of the positive disease samples, thereby bringing the points closer to the diagonal line. Similar to our observation with the APTOS 2019 fundus image collection, the data points came increasingly closer to the diagonal line for the Set-80 dataset compared to Set-20, Set-40, and Set-60 datasets.

Fig. 10 shows the confusion matrices obtained using the uncalibrated and calibrated probabilities at their default and PR-guided thresholds for the Set-20, Set-40, Set-60, and Set-80 datasets, respectively, constructed from the Shenzhen TB CXR collection. The confusion matrices obtained with simulated class-imbalanced datasets constructed from the Shenzhen TB CXR collection demonstrated similar characteristics to those observed with the APTOS 2019 fundus image collection. From Fig. 10, we observed that, at the default operating threshold of 0.5, the performance obtained with the calibrated probabilities in terms of recall and MCC metrics using the respective best-performing calibration method for Set-20, Set-40, Set-60, and Set-80 datasets, is significantly superior ( $p < 0.05$ ) compared to that obtained with the baseline, uncalibrated model. This underscores the fact that calibration helped to significantly improve classification performance ( $p < 0.05$ ) at the default operating threshold of 0.5. However, using the PR-guided threshold, the classification performance obtained using the calibrated probabilities is not significantly superior ( $p > 0.05$ ) compared to that obtained using the PR-guided threshold derived from uncalibrated probabilities. However, the PR-guided threshold value is observed to be significantly different ( $p < 0.05$ ) for the uncalibrated and calibrated probabilities.



**Fig. 9.** Reliability diagrams with their corresponding ECE metrics obtained using the uncalibrated and calibrated probabilities for Set-20, Set-40, Set-60, and Set-80 datasets, respectively, constructed from the

**Shenzhen TB CXR collection.** Yellow bars represent calibration errors. In the figure, (a) Set-20-baseline; (b) Set-20-Spline calibration; (c) Set-40-baseline; (d) Set-40-Beta calibration; (e) Set-60-baseline; (f) Set-60-Beta calibration; (g) Set-80-baseline; (h) Set-80-Beta calibration.



**Fig. 10.** Confusion matrices obtained with the uncalibrated and calibrated probabilities (from left to right) for (a) Set-20 dataset : Baseline ( $t_{PR} = 0.5$ ), Baseline ( $t_{PR-opt} = 0.1632$ ), Spline calibration ( $t_{PR} = 0.5$ ), and Spline calibration ( $t_{PR-opt} = 0.4701$ ), respectively; (b) Set-40 dataset: Baseline ( $t_{PR} = 0.5$ ), Baseline ( $t_{PR-opt} = 0.2776$ ), (c) Beta calibration ( $t_{PR} = 0.5$ ), and Beta calibration ( $t_{PR-opt} = 0.3458$ ), respectively; (c) Set-60 dataset: Baseline ( $t_{PR}$

= 0.5), Baseline ( $t_{PR-opt} = 0.5177$ ), Beta calibration ( $t_{PR} = 0.5$ ), and Beta calibration ( $t_{PR-opt} = 0.3505$ ), respectively; (d) Set-80 dataset: Baseline ( $t_{PR} = 0.5$ ), Baseline ( $t_{PR-opt} = 0.6338$ ), Beta calibration ( $t_{PR} = 0.5$ ), and Beta calibration ( $t_{PR-opt} = 0.3753$ ), respectively.

## 4. Discussion and conclusion:

We critically analyze and interpret the findings of our study as given below:

### 4.1. Model selection:

The method of selecting the most appropriate models from a collection of candidate models depends on the size, type, characteristics, and behavior of the data. It is worth noting that the DL models are pretrained on a large-scale collection of natural photographic images whose visual characteristics are distinct from medical images [16]. These models differ in several characteristics such as architecture, hyper-parameters, and learning strategies. Hence, they learn different feature representations from the data. For medical image classification tasks with sparse data availability, deeper models are not always optimal since they may overfit the training data and demonstrate poor generalization [2]. It is therefore indispensable that for any given medical data, the most appropriate model should be identified that could help extract meaningful feature representations and deliver superior classification performance. In this study, we experimented with several DL models that delivered SOTA performance on medical image classification tasks and selected the best model that delivered superior performance when evaluated with the hold-out test set.

While using the best model for a given dataset, we observed that the performance with the hold-out test set improved with an increase in class balance. These observations hold for both APTOS 2019 fundus and Shenzhen TB CXR image collections. The model delivered increasing recall values with an increasing number of positive abnormal samples in the training set. This shows the model learned meaningful feature representations from the additional training samples in the positive abnormal class to correctly classify more abnormalities in the test set.

### 4.2. Simulating data imbalance:

A review of the literature shows several studies that analyze the effect of calibration in a model trained with fixed-size data [9], [14], [15]. Until the time of writing this manuscript, to the best of our knowledge, we observed that no literature is available that exploring the relationship between the calibration methods, degree of class imbalance, and model performance. Such an analysis would be significant, particularly considering medical image classification tasks, where there exist issues such as low volume of disease samples and limited availability of expert annotations. In this study, we simulated class imbalance by divided a balanced dataset into multiple datasets with varying degrees of imbalance of the positive disease samples. We observed that different calibration methods delivered superior calibration performance with different datasets. This underscores the fact that the performance obtained with a given calibration method depends on the existing relationship between the predicted probabilities and the fraction of positive disease samples and if that calibration method would help map these uncalibrated probabilities to the true likelihood of occurrence of these samples.



### 4.3. AUROC and AUPRC values before and after calibration:

We observed that the value of AUROC and AUPRC didn't change before and after calibration, irrespective of the calibration method. This is because AUROC and AUPRC are measures of discrimination. These are rank measures that help to analyze if the observations are put in the best possible order. However, such analyses do not ensure that the predicted probabilities would represent the true occurrence likelihood of events. On the other hand, calibration applies a transformation to map the uncalibrated probabilities to their true occurrence likelihood while maintaining the rank order, hence, the AUC and AUPRC values remained unchanged after calibration.

### 4.4. Relationship between the ECE metric and class imbalance:

We observed that the statistical significance of ECE and log loss reduced with an increase in class balance. That is, the ECE and log loss achieved with calibrated probabilities for the Set-20 and Set-40 datasets were significantly smaller ( $p < 0.05$ ) compared to that obtained using the uncalibrated probabilities. This observation holds with both APTOS 2019 fundus and Shenzhen TB CXR image collections. However, with increasing class balance, as with the Set-60 and Set-80 datasets, the ECE and log loss obtained with calibrated probabilities were markedly but not significantly smaller ( $p > 0.05$ ) compared to that obtained using uncalibrated probabilities. This led to the observation that calibration methods help reduce calibration error, however, the significance of this decrease in ECE and log loss reduced with an increase in class balance. Fig.11 shows a plot of ECE measured with the uncalibrated and calibrated probabilities against the respective datasets. We observed that the ECE measured with uncalibrated and calibrated probabilities did not constantly decrease with an increase in class balance. This shows that no conclusive relationship exists between the calibration error and the class imbalance in the dataset.

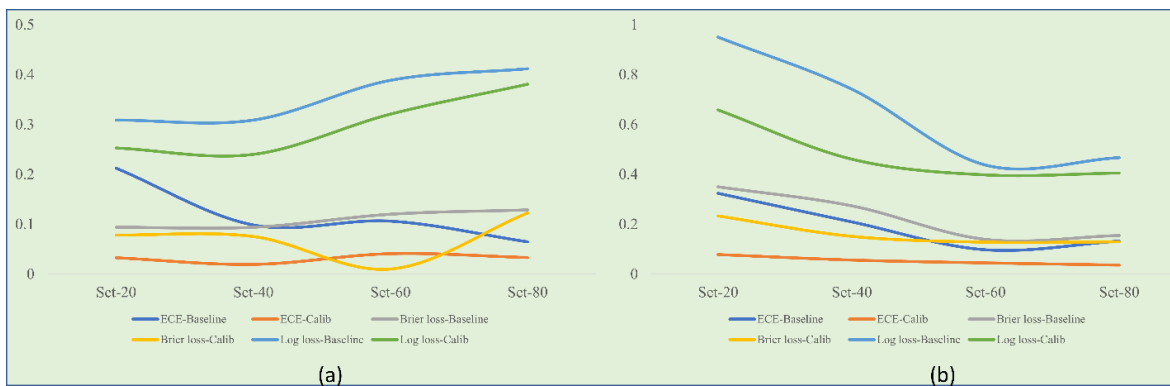


Fig. 11. A plot of ECE values (in the y-axis) and the datasets of varying class imbalances (in the x-axis).

### 4.5. PR-guided threshold and model performance:

Unlike ROC curves, the PR curves focus on model performance for the positive disease class samples that are low volume, high-impact events in a classification task. Hence, they are

more useful where the positive disease class is significant compared to the negative class and are more informative than the ROC curves, particularly in imbalanced classification tasks [29]. We aimed to (i) identify an optimal PR-guided threshold derived from calibrated probabilities for varying degrees of data imbalances and (ii) investigate if the classification performance obtained with these thresholds would be significantly superior ( $p < 0.05$ ) compared to that obtained using the PR guided threshold derived from uncalibrated probabilities.

We observed that, at the default operating threshold of 0.5, the classification performance achieved with the calibrated probabilities using their respective best-performing calibration method is significantly superior ( $p < 0.05$ ) compared to that obtained with the uncalibrated probabilities. This holds when experimenting with the class-imbalance simulated datasets from both APTOS 2019 fundus and Shenzhen TB CXR image collections. This underscores the fact that, at the default operating threshold of 0.5, calibration helped to significantly improve classification performance. However, literature studies reveal that adopting the theoretical threshold of 0.5 may adversely impact performance in class imbalanced classification tasks that is common with medical images where the abnormal samples are considered rare events [25], [26]. Hence, we derived the optimal threshold from the PR curves that maximize the F-score to deliver superior performance compared to that obtained using the theoretical threshold of 0.5. We observed that using the performance achieved using the PR-guided threshold derived from calibrated probabilities is not significantly superior ( $p > 0.05$ ) compared to that using the PR-guided threshold derived from uncalibrated probabilities. However, this optimal PR-guided threshold value differed significantly ( $p < 0.05$ ) for uncalibrated and calibrated probabilities.

It is important to note that calibration does not necessarily improve performance because that is not its purpose. Literature studies report that at times, the performance of the model reduces after calibration [31]. We observed similar results when experimenting with the Set-60 dataset constructed from the Shenzhen TB CXR collection. Thus, it is possible to have a trade-off between performance and calibration. Calibration could be used as a tool to optimize model performance to represent the true likelihood of class occurrence. The optimal performance of any model, however, trained for different class imbalances, can be obtained based on threshold selection that could be guided by calibration.

The limitations of this study are: (i) We evaluated the performance of VGG-16, DenseNet-121, and Inception-V3 models toward classifying the datasets discussed in this study. With several DL models with varying architectural diversity being reported in the literature in recent times, future studies could focus on using multiple DL models and perform ensemble learning to learn improved predictions compared to any individual constituent model. (ii) We used PR curves to find the optimal threshold, however, there are other alternatives including ROC curve-based methods and manual threshold tuning. The effect of the optimal threshold obtained from these methods on the classification performance is an open research avenue. (iii) We used Platt scaling, beta calibration, and spline calibration methods in this study. However, we didn't use other popular calibration methods such as isotonic regression since we had limited data and our pilot studies showed overfitting with the use of isotonic regression-based calibration. This observation is

identical to the results reported in the literature [32]. (iv) We explored calibration performance with individual calibration methods. With a lot of research happening in calibration, new calibration algorithms and an ensemble of calibration methods may lead to improved calibration performance. (v) Calibration is used as a post-processing tool in this study to map the uncalibrated probabilities to the true occurrence likelihood. Future research could focus on custom loss measures that could incorporate calibration into the training process thereby alleviating the need for explicit training toward calibration.

### **Author Contributions:**

Conceptualization, S.R., P.G., and S.A.; methodology, S.R., P.G., and S.A.; software, S.R. and P.G.; validation, S.R.; formal analysis, S.R., and S.A.; investigation, S.R., and S.A.; resources, S.A.; data curation, S.R.; writing—original draft preparation, S.R.; writing—review and editing, S.R., P.G., and S.A.; visualization, S.R.; supervision, S.A.; project administration, S.A.; funding acquisition, S.A.

### **Funding:**

This research was supported by the Intramural Research Program of the National Library of Medicine, National Institutes of Health.

### **Data Availability Statement:**

All data supporting the findings of this study are publicly available and are cited in the manuscript.

### **Conflicts of Interest:**

The authors declare no conflict of interest.

### **References:**

1. Sahiner B, Pezeshk A, Hadjiiski LM, Wang X, Drukker K, Cha KH, Summers RM, Giger ML. Deep learning in medical imaging and radiation therapy. *Med Phys*. 2019 Jan;46(1):e1-e36. doi: 10.1002/mp.13264. Epub 2018 Nov 20. PMID: 30367497.
2. Rajaraman S, Sornapudi S, Alderson PO, Folio LR, Antani SK. Analyzing inter-reader variability affecting deep ensemble learning for COVID-19 detection in chest radiographs. *PLoS One*. 2020 Nov 12;15(11):e0242301. doi: 10.1371/journal.pone.0242301. PMID: 33180877; PMCID: PMC7660555.
3. Gulshan V, Peng L, Coram M, Stumpe MC, Wu D, Narayanaswamy A, Venugopalan S, Widner K, Madams T, Cuadros J, Kim R, Raman R, Nelson PC, Mega JL, Webster DR. Development and Validation of a Deep Learning Algorithm for Detection of Diabetic Retinopathy in Retinal Fundus Photographs. *JAMA*. 2016 Dec 13;316(22):2402-2410. doi: 10.1001/jama.2016.17216. PMID: 27898976.
4. Guo P, Xue Z, Mtema Z, Yeates K, Ginsburg O, Demarco M, Long LR, Schiffman M, Antani S. Ensemble Deep Learning for Cervix Image Selection toward Improving Reliability in

- Automated Cervical Precancer Screening. *Diagnostics* (Basel). 2020 Jul 3;10(7):451. doi: 10.3390/diagnostics10070451. PMID: 32635269; PMCID: PMC7400120.
5. Zamzmi G, Hsu LY, Li W, Sachdev V, Antani S. Harnessing Machine Intelligence in Automatic Echocardiogram Analysis: Current Status, Limitations, and Future Directions. *IEEE Rev Biomed Eng.* 2021;14:181-203. doi: 10.1109/RBME.2020.2988295. Epub 2021 Jan 22. PMID: 32305938; PMCID: PMC8077725.
  6. Qu W, Balki I, Mendez M, Valen J, Levman J, Tyrrell PN. Assessing and mitigating the effects of class imbalance in machine learning with application to X-ray imaging. *Int J Comput Assist Radiol Surg.* 2020 Dec;15(12):2041-2048. doi: 10.1007/s11548-020-02260-6. Epub 2020 Sep 23. PMID: 32965624.
  7. Ganesan P, Rajaraman S, Long R, Ghoraani B, Antani S. Assessment of Data Augmentation Strategies Toward Performance Improvement of Abnormality Classification in Chest Radiographs. *Annu Int Conf IEEE Eng Med Biol Soc.* 2019 Jul;2019:841-844. doi: 10.1109/EMBC.2019.8857516. PMID: 31946026.
  8. Fujiwara K, Huang Y, Hori K, Nishioji K, Kobayashi M, Kamaguchi M, Kano M. Over- and Under-sampling Approach for Extremely Imbalanced and Small Minority Data Problem in Health Record Analysis. *Front Public Health.* 2020 May 19;8:178. doi: 10.3389/fpubh.2020.00178. PMID: 32509717; PMCID: PMC7248318.
  9. Chuan G, Geoff P, Yu S, Weinberger, KQ: On Calibration of Modern Neural Networks. *ICML 2017*: 1321-1330
  10. Jiang X, Osl M, Kim J, Ohno-Machado L. Calibrating predictive model estimates to support personalized medicine. *J Am Med Inform Assoc.* 2012 Mar-Apr;19(2):263-74. doi: 10.1136/amiajnl-2011-000291. Epub 2011 Oct 7. PMID: 21984587; PMCID: PMC3277613.
  11. Niculescu-Mizil, A, Caruana R. Predicting good probabilities with supervised learning. *ICML 2005*: 625-632
  12. Kull M, Filho TMS, Flach PA. Beta calibration: a well-founded and easily implemented improvement on logistic calibration for binary classifiers. *AISTATS 2017*: 623-631
  13. Lucena B. Spline-Based Probability Calibration. *CoRR abs/1809.07751* (2018)
  14. Nixon J, Dusenberry M, Jerfel G, Nguyen T, Liu J, Zhang L, Tran D. Measuring Calibration in Deep Learning. *ArXiv preprint. arXiv:1904.01685 [cs.LG]*
  15. Liang, G Zhang Y, Wang X, Jacobs N. Improved Trainable Calibration Method for Neural Networks on Medical Imaging Classification. *CoRR abs/2009.04057* (2020)
  16. Krizhevsky A, Sutskever I, Hinton GE. ImageNet classification with deep convolutional neural networks. *Commun. ACM* 60(6): 84-90 (2017)
  17. He K, Zhang X, Ren S, Sun J. Deep Residual Learning for Image Recognition. 2016 IEEE Conference on Computer Vision and Pattern Recognition (CVPR), 2016, pp. 770-778, doi: 10.1109/CVPR.2016.90.
  18. Huang G, Liu Z, van der Maaten L, Weinberger KQ. Densely Connected Convolutional Networks. *CVPR 2017*: 2261-2269

19. Iandola FN, Moskewicz MW, Ashraf K, Han S, Dally WJ, Keutzer K. SqueezeNet: AlexNet-level accuracy with 50x fewer parameters and <1MB model size. CoRR abs/1602.07360 (2016)
20. Carneiro G, Zorron Cheng Tao Pu L, Singh R, Burt A. Deep learning uncertainty and confidence calibration for the five-class polyp classification from colonoscopy. *Med Image Anal.* 2020 May;62:101653. doi: 10.1016/j.media.2020.101653. Epub 2020 Feb 28. PMID: 32172037.
21. Pollastri F, Maroñas J, Bolelli F, Ligabue G, Paredes R, Magistroni R, Grana C. Confidence Calibration for Deep Renal Biopsy Immunofluorescence Image Classification. ICPR 2020: 1298-1305
22. Jaeger S, Candemir S, Antani S, Wáng YX, Lu PX, Thoma G. Two public chest X-ray datasets for computer-aided screening of pulmonary diseases. *Quant Imaging Med Surg.* 2014;4(6):475-477. doi:10.3978/j.issn.2223-4292.2014.11.20
23. Simonyan K, Zisserman A. Very Deep Convolutional Networks for Large-Scale Image Recognition. ICLR 2015.
24. Szegedy C, Vanhoucke V, Ioffe S, Shlens J, Wojna Z. Rethinking the Inception Architecture for Computer Vision. CVPR 2016: 2818-2826
25. Esposito C, Landrum GA, Schneider N, Stiefl N, Riniker S. GHOST: Adjusting the Decision Threshold to Handle Imbalanced Data in Machine Learning. *J Chem Inf Model.* 2021 Jun 28;61(6):2623-2640. doi: 10.1021/acs.jcim.1c00160. Epub 2021 Jun 8. PMID: 34100609.
26. He H, Ma, Y. Imbalanced Learning: Foundations, Algorithms, and Applications. Wiley – IEEE Press.
27. Wang D, Feng Y, Attwood K, Tian L. Optimal threshold selection methods under tree or umbrella ordering. *J Biopharm Stat.* 2019;29(1):98-114. doi: 10.1080/10543406.2018.1489410. Epub 2018 Jun 25. PMID: 29939828.
28. Böhning D, Böhning W, Holling H. Revisiting Youden's index as a useful measure of the misclassification error in meta-analysis of diagnostic studies. *Stat Methods Med Res.* 2008 Dec;17(6):543-54. doi: 10.1177/0962280207081867. Epub 2008 Mar 28. PMID: 18375457.
29. Flach PA, Kull M. Precision-Recall-Gain Curves: PR Analysis Done Right. NIPS 2015: 838-846
30. Lin, HT., Lin, CJ. & Weng, R.C. A note on Platt's probabilistic outputs for support vector machines. *Mach Learn* 68, 267–276 (2007). <https://doi.org/10.1007/s10994-007-5018-6>
31. Cohen I, Goldszmidt M. Properties and Benefits of Calibrated Classifiers. In: Boulicaut JF, Esposito F, Giannotti F, Pedreschi D. (eds) Knowledge Discovery in Databases: PKDD 2004. Lecture Notes in Computer Science, vol 3202. Springer, Berlin, Heidelberg. [https://doi.org/10.1007/978-3-540-30116-5\\_14](https://doi.org/10.1007/978-3-540-30116-5_14)
32. Jiang X, Osl M, Kim J, Ohno-Machado L. Smooth isotonic regression: a new method to calibrate predictive models. *AMIA Jt Summits Transl Sci Proc.* 2011;2011:16-20. Epub 2011 Mar 7. PMID: 22211175; PMCID: PMC3248752.